Chem. Res. Chinese Universities, 2019, 35(2), 261—270 doi: 10.1007/s40242-019-8316-1

Freeze-drying-assisted Synthesis of Mesoporous $CoMoO_4$ Nanosheets as Anode Electrode Material for Enhanced Lithium Batteries

WANG Wei[1*], WANG Tao[1], FAN Xuecheng[1], ZHANG Cuilin[1], HU Jinxing[1], CHEN Hui[1], FANG Zhenxing[1], YAN Jiefeng[1] and LIU Bing[2*]

1. College of Science & Technology, Ningbo University, Ningbo 315212, P. R. China;

2. State Key Laboratory of Bio-Fibers and Eco-Textiles, Qingdao University, Qingdao 266071, P. R. China

Abstract A facile and green freeze-drying-assisted method was proposed to synthesize $CoMoO_4$ mesoporous nanosheets(MPNSs). The resulting product exhibits a high specific capacity and good rate performance when evaluated as an anode material for lithium-ion batteries(LIBs). The reversible specific capacity can be kept at 1105.2 $mA\cdot h\cdot g^{-1}$ after 100 cycles at a current density of 0.2 A/g. Even at the current densities of 1 and 4 A/g, the $CoMoO_4$ MPNSs electrode can still retain the reversible capacities of 1148.7 and 540 $mA\cdot h\cdot g^{-1}$, respectively. Furthermore, the full cell($LiFePO_4$ cathode/$CoMoO_4$ MPNSs anode) displays a stable discharge capacity of 146.7 $mA\cdot h\cdot g^{-1}$ at 0.1 C (1 C=170 mA/g) together with an initial coulombic efficiency of 98.2%. In addition, the $CoMoO_4$ crystal structure is destroyed and reduced into Co^0 and Mo^0 in the first discharge process. In the subsequent cycles, the attractive Li storage properties come from the reversible conversions between Co/Co^{2+} and Mo/Mo^{6+}. The improved electrochemical performance of $CoMoO_4$ MPNSs is mainly attributed to their unique porous structures, which not only possess a good ion diffusion and electronic conduction pathway, but also provide many cavities to alleviate the volume changes during repeated cycling. This work offers a new perspective to the design of other porous electrode materials with a good energy storage performance.

Keywords Freeze-drying; Mesoporous nanosheet; $CoMoO_4$; Anode material; Lithium storage

1 Introduction

An ever-increasing demand for electric vehicles and portable electronic devices has been driving the rapid development for lithium-ion batteries(LIBs)[1]. The electrochemical properties of LIBs are mainly dominated by their electrode materials[2,3]. Molybdenum trioxide(MoO_3) can be considered as one prospective electrode material due to its intriguing layered structure associated with multiple valence states(ranging from 3^+ to 6^+) and high thermal and chemical stability[4]. On the one hand, the layered crystal structure favors the reversible inserting/extracting process of Li^+ into/from the MoO_3 frameworks. This process is highly kinetically favorable and would not cleave the Mo—O bonds. Into one MoO_3 molecule can reversibly insert at most 1.5 lithium atoms, which contributes a theoretical capacity of *ca.* 280 $mA\cdot h\cdot g^{-1}$ at 1.5—3.5 V *vs.* Li^+/Li[5]. Thus MoO_3 can be used as the cathode material in LIBs. On the other hand, MoO_3 can also be used as a conversion-type anode material for LIBs. During the redox reaction, MoO_3 can reversibly react with 4—6 mol of Li, so a theoretical capacity of 745—1117 $mA\cdot h\cdot g^{-1}$ can be acquired at 0—3 V[6]. Recently, because of the multitudinous valence states, intricate chemical compositions and synergetic effects in multicomponent molybdenum-based oxide, various metal molybdates(such as $XMoO_4$, where X=Ca, Mg, Fe, Co, Ni, Mn, Zn, Cd) have been explored to promote the Li-cycling properties[7—14].

$CoMoO_4$, as one of the metal molybdates, has attracted more and more research interests because of its characteristic properties in magnetism, photocatalysis and electrochemistry[15]. There are three basic polymorphs of $CoMoO_4$, *i.e.*, α-phase $CoMoO_4$(α-$CoMoO_4$), β-allomerism(β-$CoMoO_4$) and $CoMoO_4\cdot nH_2O$, in which α-$CoMoO_4$ is the thermodynamically stable phase that can be obtained at lower temperatures. In α-$CoMoO_4$, the Co and Mo atoms are both at octahedral sites,

*Corresponding authors. Email: wangwei4@nbu.edu.cn; bing_liu@qdu.edu.cn

Received September 28, 2018; accepted December 25, 2018.

Supported by the Natural Science Foundation of Zhejiang Province, China(No.LQ18B010001), the Scientific Research Fund of Zhejiang Provincial Education Department, China(Nos.Y201737041, Y201839092), the Scientific Research Fund of Ningbo City, China(Nos.2018A610083, 2017A610299), the Scientific Research Fund of Ningbo University, China(Nos.XYL17007, 2018SRIP0041), the National College Students' Innovation and Entrepreneurship Training Program, China(No.201813277003), the National Natural Science Foundation of China(No.21701095), the Natural Science Foundation of Shandong Province, China(No.ZR2017BEM007), the China Postdoctoral Science Foundation(No.2017M622131) and the Program of Science and Technology for Higher Education in Shandong Province, China(No.J17KA010).

which is the same as the Mo atoms in MoO_3 oxide. Thus the electronic properties of α-$CoMoO_4$ are similar to those of MoO_3[8]. In virtue of the above similarities, Yu *et al*.[15] synthesized α-$CoMoO_4$ microcrystals *via* a facile hydrothermal method and studied its cathodic performance(reversible specific capacity of 130 $mA\cdot h\cdot g^{-1}$) at 1.2—4.0 V. In 2013, for the first time, Chowdari *et al*.[8] exploited a polymer precursor method to synthesize α-$CoMoO_4$ submicrometer particles and reported its anodic behavior in a range of 0.005—3.0 V. Since then, owing to its good properties, α-$CoMoO_4$ has attracted more and more attentions as one kind of potential anode electrode. For example, Yan *et al*.[16] successfully fabricated $CoMoO_4$ nanosheets on nickel foam by a solution-based method, and the as-prepared nanosheets presented a charge capacity of 894 $mA\cdot h\cdot g^{-1}$. Kang *et al*.[17,18] prepared $CoMoO_4$ microspheres by dint of ultrasonic spray pyrolysis, and the microspheres as LIB anodes exhibited a good cycling stability. Recently, Guo *et al*.[19] reported a solvothermal method using SiO_2 nanospheres as sacrificial template for synthesizing $CoMoO_4$ hollow nanostructures, and the hollow spheres displayed a reversible capacity of 1066 $mA\cdot h\cdot g^{-1}$ after 200 cycles.

Moreover, for the sake of enhancing the electrical/ionic conductivity and mechanical stability for $CoMoO_4$ electrodes, various carbon based materials have been explored, such as $CoMoO_4$ nanoparticles/graphene[20], $CoMoO_4$ nanorods/graphene[21,22], $CoMoO_4$ nanofibers@graphene[23], $CoMoO_4$ nanospheres/graphene[24], $CoMoO_4$/polypyrrole nanowire[25], $CoMoO_4$ nanosheets on flexible carbon fabric[26], and improved lithium storage performance has been achieved. In addition, because of the specific synergy, constructing heterostructure is supposed to be another available approach for gaining high electronic conductivity and improving the cycling stability. As a consequence, many attempts have been made to design and manufacture $CoMoO_4$-based hybrid, such as carbon-coated Co_3O_4/$CoMoO_4$ nanospheres[27], $CoMoO_4$/Fe_2O_3 core-shell nanorods[28], and $CoMoO_4$/Co_3O_4 hollow porous octahedrons[29]. And the products showed an enhanced Li-storage performance. From the above reports, it can be observed that several approaches have been exploited for synthesizing different $CoMoO_4$ frameworks, primarily containing solution-based precipitation[20,21,29], hard-template[19], solid-state reaction[8], ultrasonic nebulization[17,18], electrospinning[23], and hydrothermal method[16,22,24—28] followed by a calcination process at a high temperature. However, it is still an enormous challenge to explore an efficient and time-saving approach for fabricating $CoMoO_4$, and to control and regulate the morphology for optimizing its practical application for Li-storage[30].

Herein, a freeze-drying assisted method was proposed for the first time to synthesize $CoMoO_4$ mesoporous nanosheets(MPNSs). This is a facile and waste-free strategy. The reasons are as follows. In contrast with previous methods, the freeze-drying method can guarantee the uniform mixing of the cobalt and molybdenum sources at the atomic or molecular levels, then enhance their reaction activities in the annealing process, and thus help to lower the annealing temperature, shorten the heating time, decrease the particle size and increase the crystallinity[31,32]. Furthermore, the current approach does not make use of any templates or surfactants, which is more efficient and time-saving, and also does not need a post-washing procedure, thus no solid wastes form. During the process of pyrolysis in our work, the organic functional groups in the raw materials decomposed into a variety of gases, and simultaneously the metal contained precursors gradually crystallized into uniform $CoMoO_4$ nanoparticles(NPs) with an approximate of 30 nm in diameter, producing the final $CoMoO_4$ MPNSs. The mesoporous nanosheets(NSs) structure can not only be favorable for fast Li^+ and e^- transport, but also alleviate large volume changes during the lithiation/delithiation process. When evaluated as an anode electrode for LIBs, the $CoMoO_4$ MPNSs show an enhanced Li-storage property in terms of reversible capacity, cycling durability and rate performance. Besides, the $LiFePO_4$/$CoMoO_4$ MPNSs full cell affords a stable reversible capability(146.7 $mA\cdot h\cdot g^{-1}$ at 0.1 C) and good cyclic stability.

2 Experimental

2.1 Synthesis of $CoMoO_4$ MPNSs

In a typical synthesis of $CoMoO_4$ MPNSs, cobaltous acetate tetrahydrate[$Co(Ac)_2\cdot 4H_2O$, 0.249 g, 1 mmol, Aldrich] and hexaammonium molybdate tetrahydrate[$(NH_4)_6Mo_7O_{24}\cdot 4H_2O$, 0.176 g, 0.143 mmol, Aldrich] were dissolved in 10 mL of distilled water(Ningbo Chemical Reagent Ltd.) to form a palm red solution. This transparent solution was then freeze-dried for 48 h, and a light pink fluffy floc was formed. The freeze-drying can ensure the homogeneous distribution of constituent ions, thus avoiding the phase separation and favouring the crystallization during calcining process. Finally, the pink fluffy floc was heated under N_2 atmosphere at 500 °C and a heating rate of 1 °C/min for 3 h. The control sample(bare $CoMoO_4$) was prepared by replacing $Co(Ac)_2\cdot 4H_2O$ with cobalt chloride hexahydrate($CoCl_2\cdot 6H_2O$) under other conditions being the same as those for preparing $CoMoO_4$ MPNSs.

2.2 Characterization

A JSM-6330F microscope was employed to provide the scanning electron microscopy(SEM) and element mapping measurement. A JEOL-2100F microscope was adopted to give the transmission electron microscopy(TEM), high resolution transmission electron microscopy(HRTEM) and selected-area electron diffraction(SAED) test. The microscope was operated at 200 kV. A Bruker D8 X-ray powder diffractometer was used to measure the X-ray powder diffraction(XRD) patterns, which was performed at 40 kV and 40 mA. An accelerated surface area and porosimetry instrument(ASAP2020) was employed to obtain the specific surface area and pore volume. The Barrett-Joyner-Halenda(BJH) model was used to analyse the pore size distribution(PSD) plot by the adsorption isotherm branch. An ESCALab 220i-XL electron spectrometer was adopted to perform the X-ray photoelectron spectroscopy(XPS) measurement. The freeze-drying was carried out on a Freeze Drier(Alpha1-4LDplus, Christ).

2.3 Electrochemical Measurement

The obtained samples were used as anode materials and assembled into 2025 coin cells. To prepare the working electrode, $CoMoO_4$ MPNSs, carbon black, and sodium carboxymethyl-cellulose(CMC) binder were mixed at a mass ratio of 80:10:10. And the obtained slurry was scraped onto a copper foil, which was then dried at 120 °C for 36 h under vacuum. The loading mass of each electrode was 0.96—1.04 mg/cm^2. The metal lithium plate was used as the reference electrode. The separator was Celgard 2400 polypropylene membrane. $LiPF_6$(1 mol/L) was dissolved in a mixture of diethyl carbonate (DEC)/dimethyl carbonate(DMC)/ethylene carbonate(EC) (1:1:1, volume ratio). The mixture solution was used as the nonaqueous electrolyte. The coin-cell was assembled in a glove-box filled with Ar. LAND CT2001A was employed to do the galvanostatic cycling tests at room temperature and 0.01—3.0 V *vs.* Li^+/Li. CHI-650E electrochemical workstation was used to measure the cyclicvoltammogram(CV) and electrochemical impedance spectra(EIS). To collect the TEM measurements of $CoMoO_4$ MPNSs after several cycles, the anode materials were first dismantled in a glove-box, and then rinsed with DMC(Sigma-Aldrich, 99%) and absolute alcohol to eliminate the distractions from the residual electrolyte.

Furthermore, a full coin-type cell, combined with a $LiFePO_4$ cathode, a pre-lithiated $CoMoO_4$ MPNSs anode and the same electrolyte, was also assembled. The pre-lithiation of the $CoMoO_4$ MPNSs electrode as well as the approach of cell capacity balance was reported in our previously papers[32,33]. To be specific, the mass loadings of the anode and cathode electrodes were 0.96—1.04 and 3.6—4.2 mg/cm^2, respectively. The full cell capacity was calculated on the cathode side, and the battery was cycled at 0.1C(1C=170 mA/g) between 1.6—3.8 V.

3 Results and Discussion

The formation process of $CoMoO_4$ MPNSs involves two steps(Scheme 1). First, a palm red transparent solution was formed by dissolving $Co(Ac)_2{\cdot}4H_2O$ and $(NH_4)_6Mo_7O_{24}{\cdot}4H_2O$ in deionized water. Then, the obtained clear solution was freeze-dried, and a light pink fluffy floc was developed. We denoted this loose intermediate product as Co-Mo-precursor. The precursor had a homogeneous dispersion of each component and displayed a sheet-like structure(Fig.S1, see the Electronic Supplementary Material of this paper). The XRD pattern(Fig.S2, see the Electronic Supplementary Material of this paper) of the precursor exhibited an abroad-hump shape. This is a typical amorphous structure[33]. Finally, the Co-Mo-precursor was put in N_2 atmosphere at 500 °C to accomplish crystallization and generate a $CoMoO_4$ sample. In the pyrolysis process, the organic functional groups in the precursor decomposed gradually with the increase of temperature, and evolved several gases, such as NH_3, CO_2, CO and H_2O. Simultaneously, the Co and Mo precursors were transformed into $CoMoO_4$ nanoparticles, thus leading to the formation of porous $CoMoO_4$ MPNSs.

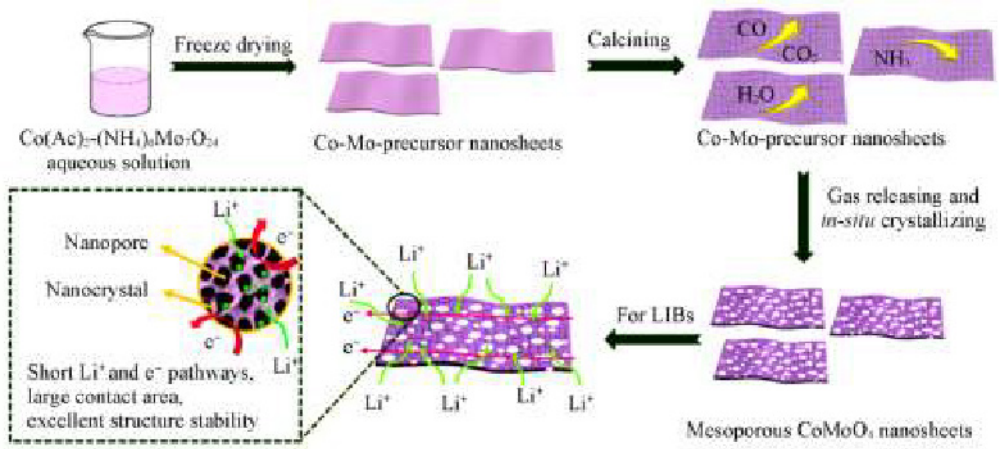

Scheme 1 Schematic diagram illustrating the procedure to fabricate $CoMoO_4$ MPNSs and the schematic representation of short Li^+ and e^- pathways, large contact area, and excellent structure stability in $CoMoO_4$ MPNSs

SEM and TEM techniques were first employed to investigate the microstructure and morphology of $CoMoO_4$ MPNSs. Fig.1(A) and (B) present the SEM images of $CoMoO_4$ MPNSs. Clearly, a macroscopic sheet-like structure is shown in Fig.1(A). From the enlarged image[Fig.1(B)], it could be seen that the surface of the sheet was constructed by small particles, and the tight NPs were throughout the whole sheet. TEM observations [Fig.1(C)] clearly displayed that the NSs were assembled from NPs. Between these NPs, numerous mesopores had been formed, which might be resulted from the evolution of large quantities of gases during the thermal treatment process. The higher-magnification TEM images[Fig.1(D), (E)] present an interconnected pore network structure with an obvious texture contrast. Moreover, the mesoporous structure belongs to worm-like pore and the size was approximate 10—30 nm. Such an interconnected porous structure might effectively prevent $CoMoO_4$ NSs from stacking together and make them possess better mechanical strength(Scheme 1). The HRTEM image [Fig.1(F)] indicates that the interlayer spacing was 0.336 nm. This is consistent with the (002) planes of monoclinic phase

α-$CoMoO_4$(JCPDS No.21-0868). The SAED pattern is shown in the inset of Fig.1(F). This result confirms the polycrystalline nature of $CoMoO_4$ MPNSs. The XRD analysis in Fig.2 demonstrates the formation of the $CoMoO_4$ phase, although the peak is relative broad and weak, indicating a small crystallite size. In addition, the uniform distributions of Co, Mo, and O elements on the whole nanosheet surface have also been proven by the elemental mappings in Fig.S3(see the Electronic Supplementary Material of this paper).

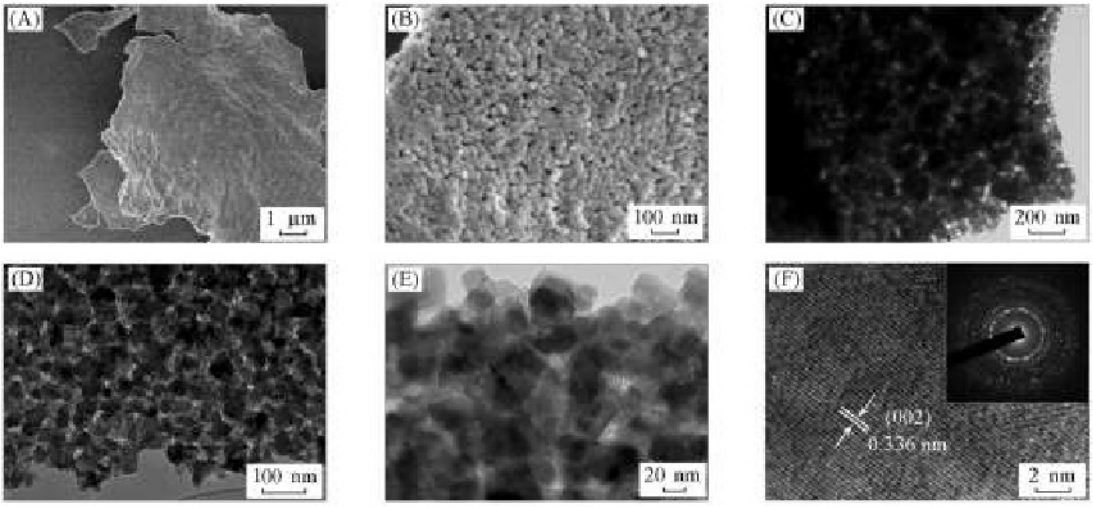

Fig.1 Typical FESEM images(A, B), TEM images(C—E) of $CoMoO_4$ MPNSs with different magnifications and HRTEM image(F) and SAED pattern(inset) of $CoMoO_4$ MPNSs

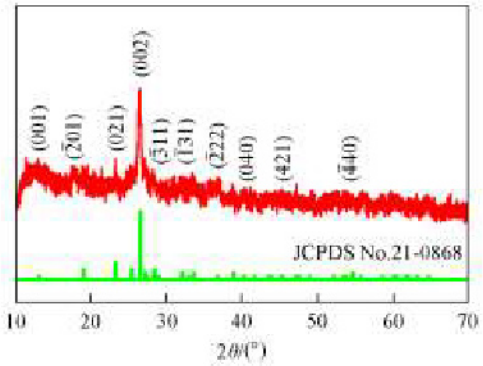

Fig.2 XRD patterns of $CoMoO_4$ MPNSs

To gain a further insight into the porous nature and the pore size distribution of $CoMoO_4$ MPNSs, N_2 adsorption measurement was performed. As shown in Fig.3, the isotherm is a typical IV-type Langmuir isotherm with a distinct hysteresis loop, revealing the mesoporous structure of $CoMoO_4$ MPNSs. $CoMoO_4$ MPNSs have a specific surface area of 28.76 m^2/g and a pore volume of 0.15 m^3/g. The pore size distribution (Fig.3, inset) shows a wide peak between 10 and 30 nm and a narrow peak centered at 21.3 nm, agreeing well with the above TEM observations. In comparison with this, the Co-Mo-400, Co-Mo-600 and bulk $CoMoO_4$(Fig.S4, see the Electronic Supplementary Material of this paper) show low surface areas of 18.07, 12.53 and 9.27 m^2/g, respectively. The pore size distributions of Co-Mo-400, Co-Mo-600 and bulk $CoMoO_4$ are also displayed in Fig.S4.

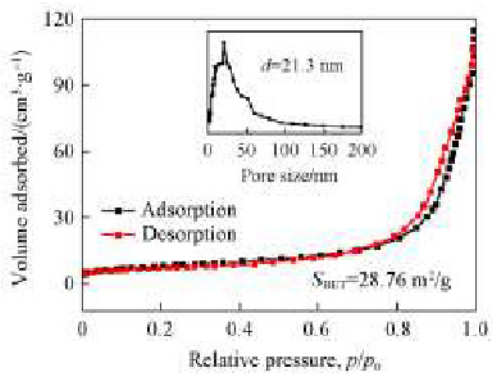

Fig.3 N_2 adsorption/desorption isotherms and BJH pore size distribution(inset) of $CoMoO_4$ MPNSs

Both Co-Mo-400 and Co-Mo-600 showed a multiple distribution between 2 and 50 nm, further confirming the existence of mesopores, while bulk $CoMoO_4$ displayed a narrow distribution between 2 and 10 nm. Such a porous structure and a large specific surface area for $CoMoO_4$ MPNSs can not only effectively shorten the diffusion pathways of Li^+ and e^- in active material but also provide a large contact area for electrolyte storage and ensuring Li^+ diffusion in channels across the whole anode, thus significantly improving the rate capability and cycling performance(as shown in Scheme 1).

In order to figure out the chemical composition and surface electronic state of $CoMoO_4$ MPNSs, X-ray photoelectron spectroscopy(XPS) was employed, with the corresponding results shown in Fig.4. The presence of Co, Mo and O elements is first verified in the survey spectrum in Fig.4(A). Fig.4(B) shows the high-resolution spectrum of Co_{2p}. As can be seen, there are two groups of peaks at 780.5, 796.2 eV and 782.2, 797.3 eV, respectively. The former peaks could be assigned to Co^{3+}, while the later peak belonged to Co^{2+}[34]. Moreover, the shake-up satellite peaks at *ca*. 786 and 802.6 eV gave a further evidence for the existence of Co_{2p}[34].

In the high-resolution XPS spectrum of Mo_{3d}[Fig.4(C)], two kinds of molybdenum species containing Mo^{4+} and Mo^{6+}

can be observed. The fitting peaks at 229.9 and 232.6 eV can be indexed to Mo^{4+}, while the fitting peaks at 232 and 235.3 eV can be indexed to Mo^{6+}[35]. Fig.4(D) shows the O_{1s} signal and it displays four types of oxygen. To be specific, the peaks at 529.8 and 530.4 eV are deemed as the lattice oxygen atoms of Co—O/Mo—O and the hydroxide ions of Co-OH/Mo-OH species. The peak at 531 eV can be attributed to an oxygen vacancy[36], while the peak at 532.3 eV is due to a small amount of physically adsorbed water molecules.

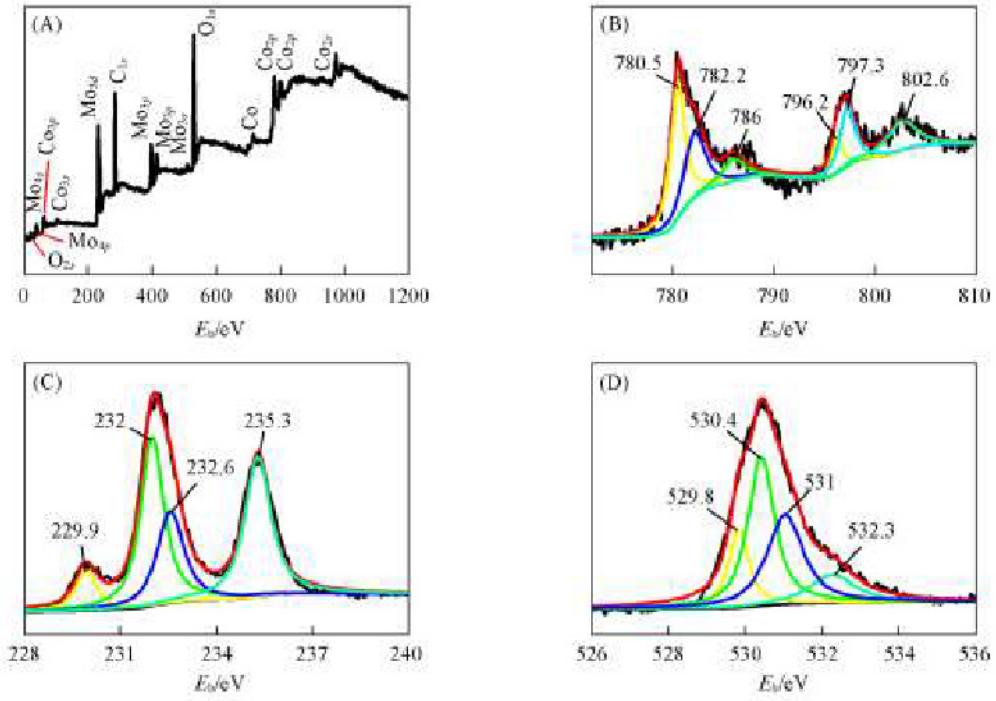

Fig.4 Full-scan XPS spectra of $CoMoO_4$ MPNSs(A), and high-resolution XPS spectra of Co_{2p}(B), Mo_{3d}(C) and O_{1s}(D)

Temperature-dependent experiments were carried out to distinguish the effect of the calcining temperature on the composition and morphology of the final product. We altered the calcination temperatures from 400 °C to 600 °C. And the resultant samples were denoted as Co-Mo-400 and Co-Mo-600, respectively. Both the above samples were studied by XRD and SEM. XRD pattern of Co-Mo-400 is first shown in Fig.S5(A)(see the Electronic Supplementary Material of this paper). It could be seen that all the diffraction peaks match well with the JCPDS No.21-0868, which is a monoclinic α-$CoMoO_4$ phase. Fig.S5(D) is the XRD pattern of Co-Mo-600. Surprisingly, except the diffraction peaks of α-$CoMoO_4$, the peaks of $Co_2Mo_3O_8$(JCPDS No.71-1423) could also be detected, which were already marked with "∗". In contrast to $CoMoO_4$, the $Co_2Mo_3O_8$ phase has a lower ratio of oxygen to molybdenum, and is a product of $CoMoO_4$ decomposition at a higher temperature[37]. Fig.S5(B) presents a low-magnification SEM image of Co-Mo-400; it reveals that this sample holds a sheet-like morphology. Fig.S5(C) is a high-magnification SEM image of Co-Mo-400. It exhibits that the sheets were assembled by small nanoparticles, which were tightly connected with each other to form numerous mesopore structures. With the increase of calcination temperature to 600 °C, the nanoparticle size got bigger and the presence of mesopore became much more obviously[Co-Mo-600, Fig.S5(E), (F)]. As a contrast, XRD and SEM were also employed to investigate the bulk $CoMoO_4$, with the results shown in Fig.S5(G)—(I).

The reaction processes of resultant products as an anode electrode were first distinguished by means of cyclic voltammetry(CV). The CV tests of $CoMoO_4$ MPNSs were performed at a scanning speed of 0.1 mV/s. Fig.5(A) shows the first five cycles of CV profiles. In the initial cathodic profile, there are three apparent reduction peaks appearing at 1.64, 0.4 and 0.17 V, respectively. The former weak peak located at 1.64 V could be assigned to the destructing of crystal texture into amorphous forms[20,21,24]. The middle broad peak centered at 0.4 V corresponds to the thorough reduction process of Mo^{4+} and Co^{2+} to metallic Mo and Co[8,17,20,23]. The final sharp peak at 0.17 V only appearing in the first lithiation profile could not be observed in the following cycles. This corresponds to some irreversible process in the electrode, for instance, the forming of solid electrolyte interface(SEI) and the decomposing of electrolyte[23]. After the first cycle, in the CV profiles, another three reduction peaks emerge, which are located approximately at 1.49, 0.8 and 0.13 V, respectively. The first peak at 1.49 V could be commonly recognized as the partial reduction of molybdenum from Mo^{6+} to Mo^{4+}, while the broad peaks at 0.8 and 0.13 V could be assigned to the complete reduction of Co^{2+} to Co and Mo^{4+} to Mo[19,21]. Remarkably, from the second cycle onwards, the reduction peak located at 0.4 V in the first cycle has been moved to 0.8 V. The positive shift of the reduction peak in the following cycles might be related to some activation process caused by the Li^+ insertion in the first cycle, indicating the slightly easier reduction in the subsequent cycles[19,21,26].

In the anodic scans, three obvious anodic peaks located at

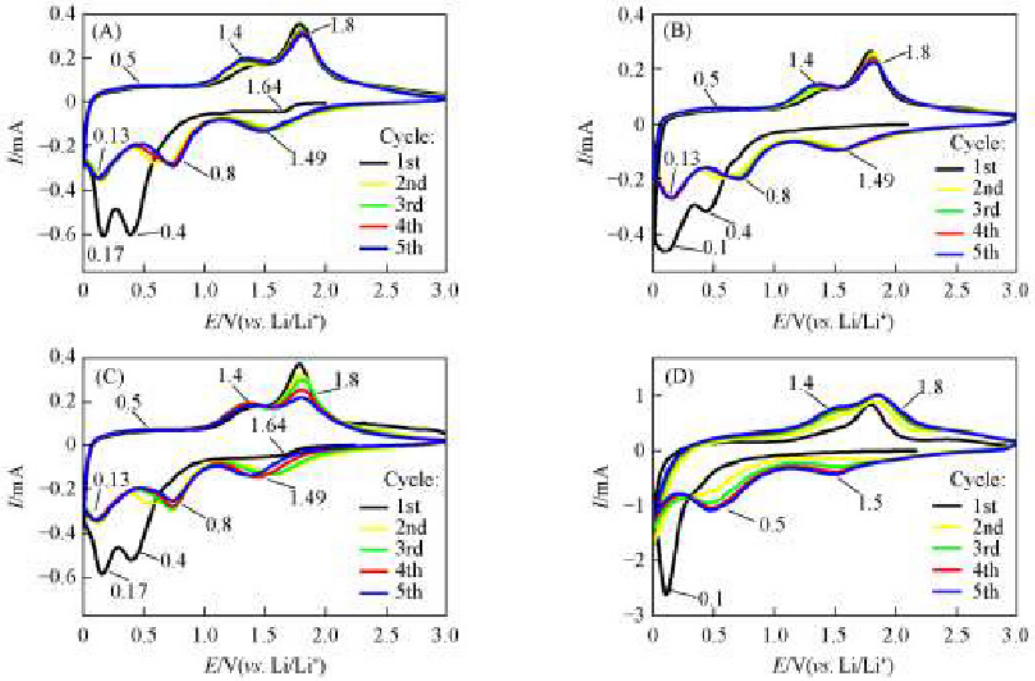

Fig.5 CV curves of different electrodes showing the first five cycles between 0.01 and 3.0 V at a scan rate of 0.1 mV/s

(A) $CoMoO_4$ MPNSs; (B) Co-Mo-400; (C) Co-Mo-600; (D) bulk $CoMoO_4$.

0.5, 1.4 and 1.8 V can be detected. The peaks at 0.5 and 1.4 V could be due to the multistep phase transition process of metal Mo to Mo^{4+}[20]. The peak at 1.8 V corresponds to the oxidation to Co^{2+} and Mo^{6+}[24]. Moreover, after the first cycle, there were three reversible oxidation/reduction pairs at 0.13/0.5, 0.8/1.4, and 1.49/1.8 V, respectively. This implied $CoMoO_4$ MPNSs favored the phase transition process and Li^+ reaction at different sites. Based on the above analysis[8], the reversible Li^+ insertion/extraction process for $CoMoO_4$ MPNSs can be summarized as follows:

$$CoMoO_4+8Li \longrightarrow Co+Mo+4Li_2O \quad (1)$$

$$Co+Li_2O \rightleftharpoons CoO+2Li \quad (2)$$

$$Mo+3Li_2O \rightleftharpoons MoO_3+6Li \quad (3)$$

Fig.5(B) and (C) show the CV curves of Co-Mo-400 and Co-Mo-600, the peaks of which are similar to those of $CoMoO_4$ MPNSs. However, with the increase of cycle number, the integral areas and peak intensities of these samples gradually decreased. This probably indicates a potential capacity fading during the continuous cycling process[20,23]. Fig.5(D) displays the CV curves of bulk $CoMoO_4$. Remarkably, compared to those of $CoMoO_4$ MPNSs, the CV curves of bulk $CoMoO_4$ are much less overlapped from the second cycle onward. These results indicate that the electrochemical reversibility of $CoMoO_4$ MPNSs sample is gradually built after the initial cycle that is much better than those of other samples.

For a full study of the Li-storage performance of $CoMoO_4$ MPNSs as an anode material for LIBs, the discharge/charge voltage profiles, operated at 0.2 A/g between 0.01—3 V, are displayed in Fig.6(A). The initial discharge profile presents an open circuit voltage(OCV) of 2.0 V and displays an apparent sloping voltage plateau starting from the OCV. With the decrease of discharge voltage to 1.0 V, the plateau declines sharply. This part corresponded to the destructing of $CoMoO_4$ crystal structure into amorphous forms and comprised a capacity of 57.5 $mA\cdot h\cdot g^{-1}$[8,18,22,23]. Then, a long sloping region can be observed up to 0.17 V, which is attributed to the complete reduction of $CoMoO_4$ to metal Mo^0 and Co^0[8,22,23]. This process contributes a capacity of 1353.1 $mA\cdot h\cdot g^{-1}$. So the discharge capacity is 1410.6 $mA\cdot h\cdot g^{-1}$ in total. During investigating the charging profile, there was a smooth voltage profile to 1.0 V. Along with the increase of recharging voltage, an upward slant voltage plateau was observed till 2.0 V, and the plateau displayed a continuous rise up to 3.0 V. This is consistent with their CV results. The initial charge capacity was 1274.4 $mA\cdot h\cdot g^{-1}$. So the $CoMoO_4$ MPNSs showed an initial coulombic efficiency(CE) as high as 90.3%. Such a high initial CE suggests the forming of a stable and thin SEI layer in $CoMoO_4$ MPNSs. This characteristic plays a key role in the real application. Furthermore, from the second cycle on, the charging and discharging curves overlapped well and there was no obvious capacity loss. This confirms the good cyclic stability of $CoMoO_4$ MPNSs. In contrast, for individual Co-Mo-400[Fig.6(B)], Co-Mo-600[Fig.6(C)] and bulk $CoMoO_4$(Fig.S6, see the Electronic Supplementary Material of this paper), all of them show much shorter discharge plateaus. Especially for Co-Mo-600, the curves faded out seriously during the whole cycles, with only a capacity of 375.4 $mA\cdot h\cdot g^{-1}$ retained. The cycling performances of the four samples($CoMoO_4$ MPNSs, Co-Mo-400, Co-Mo-600 and bulk $CoMoO_4$) at 0.2 A/g are compared in Fig.6(D).

In the case of Co-Mo-400, the reversible capacity decreased from 1428.4 $mA\cdot h\cdot g^{-1}$ to 780.7 $mA\cdot h\cdot g^{-1}$ after 100 cycles. The capacity retention ratio was 54.7% and the capacity loss ratio was 6.5% per cycle. For $CoMoO_4$ MPNSs, there was only a slight capacity loss of 136.2 $mA\cdot h\cdot g^{-1}$ during the initial cycle, yielding an irreversible loss of 9.7%. This phenomenon belonged to the SEI film forming on the surface of electrode and the Li^+ irreversible intercalation into the crystal lattice of

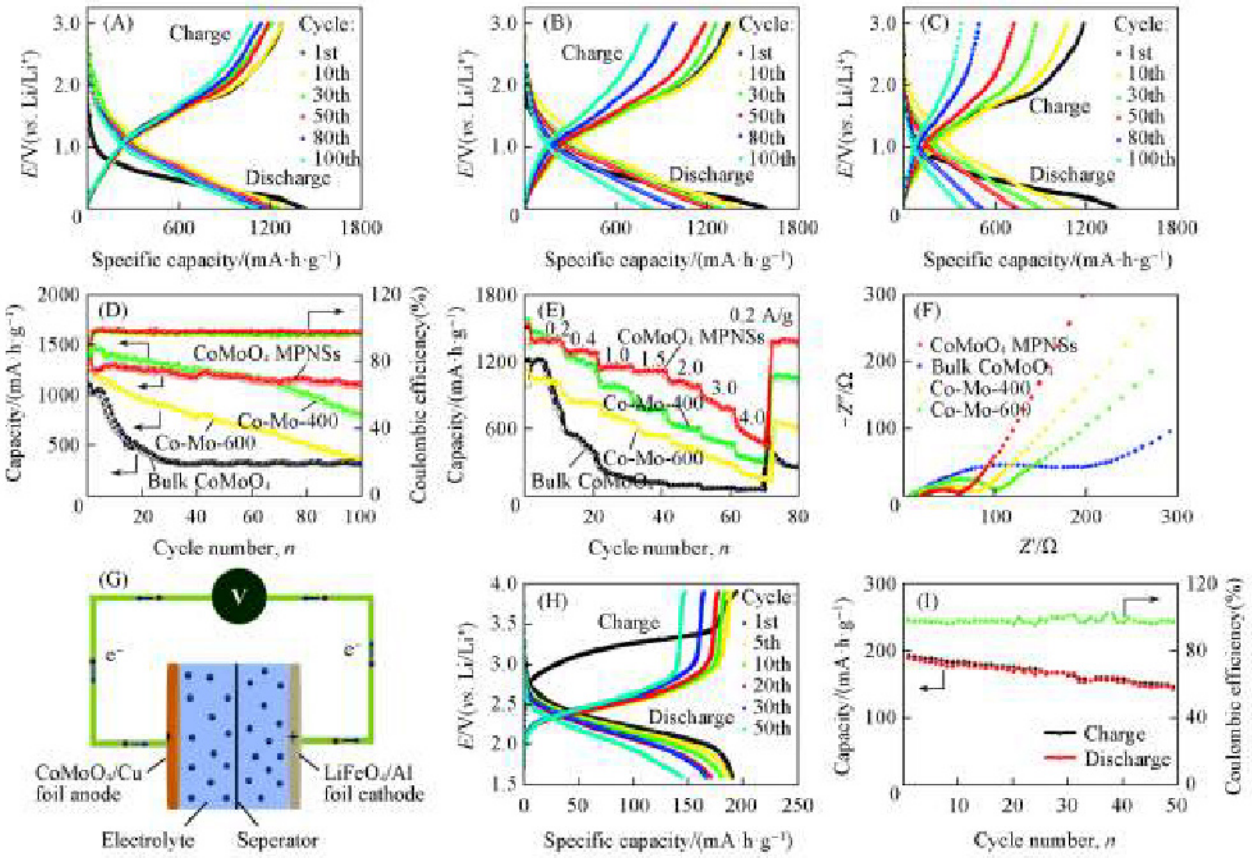

Fig.6 Discharge-charge profiles of $CoMoO_4$ MPNSs(A), Co-Mo-400(B), and Co-Mo-600(C), cycling performance and CE of $CoMoO_4$ MPNSs, Co-Mo-400, Co-Mo-600 and bulk $CoMoO_4$ cycled at 0.2 A/g(D), rate capability in a current density range of 0.2—4.0 A/g(E), Nyquist plots of $CoMoO_4$ MPNSs, Co-Mo-400, Co-Mo-600 and bulk $CoMoO_4$ after 100 cycles at 0.2 A/g(F), schematic illustration of a full cell using $CoMoO_4$ MPNSs as the anode and commercial $LiFePO_4$ as the cathode(G), voltage profiles of the full cell cycled between 1.6 and 3.8 V at 0.1C(H) and corresponding cycling performance and CE of the full cell(I)

$CoMoO_4$. From the second cycle, the specific capacity was up to 1254.6 mA·h·g^{-1} that could be retained at 1105.2 mA·h·g^{-1} after 100 cycles. $CoMoO_4$ MPNSs displayed a capacity retention ratio of 88%, and showed a much better reversibility than Co-Mo-400. For Co-Mo-600 and bulk $CoMoO_4$, their capacities faded out obviously throughout the whole cycles, and the capacity retention ratios were only 31.7% and 32.4%, respectively. These values are far lower than that of $CoMoO_4$ MPNSs. Table 1 compares the capacity of mesoporous $CoMoO_4$ nanosheets with those of the previously reported $CoMoO_4$-based materials, including various $CoMoO_4$ nano-architectures, $CoMoO_4$/carbon, $CoMoO_4$/grapheme and $CoMoO_4$/Co_3O_4 composites. $CoMoO_4$ MPNSs display a better Li storage performance when the applied current density, the cycle life

Table 1 Comparison of the capacity of present work with those of $CoMoO_4$-based materials reported

Sample	Current density/(A·g^{-1})	Cycle number	Capacity/(mA·h·g^{-1})	Ref.
Mesoporous $CoMoO_4$ nanosheet networks	0.2	100	1105.2	This work
$CoMoO_4$ microspheres	1.0	100	1023	[18]
$CoMoO_4$/Co_3O_4 hollow porous octahedrons	0.2	100	1050.3	[29]
$CoMoO_4$@graphene nanospheres	0.5	150	783	[24]
$CoMoO_4$/Fe_2O_3 core-shell nanorods	0.19	100	1236	[28]
$CoMoO_4$ hollow nanosheets	0.5	200	1066	[19]
Carbon-coated Co_3O_4/$CoMoO_4$ nanospheres	0.2	100	918	[27]
$CoMoO_4$/carbon fabric composites	0.1	150	1128.05	[26]
$CoMoO_4$@graphene nanofibers	0.1	200	735	[23]
$CoMoO_4$/PPy core-shell nanowire arrays	0.75	100	934	[25]
$CoMoO_4$ nanorods-graphene composite	0.1	40	968	[22]
$CoMoO_4$ nanorods/reduced graphene oxide	0.1	100	628	[21]
Rattle-type $CoMoO_4$ microspheres	0.5	150	1065	[17]
$CoMoO_4$ nanosheet on nickel foam	0.3	100	894	[16]
$CoMoO_4$ nanoparticles/reduced graphene oxide	0.074	50	920	[20]
$CoMoO_4$ submicrometer particles	0.098	50	940	[8]

and the capacity are comprehensively considered. Furthermore, compared with other reported approaches, the freeze-drying assisted strategy in our work is simple and high-yielding. On the one hand, it does not need any templates or surfactants, and also avoids the post-washing process. On the other hand, the freeze-dried precursor is directly sintered under N_2 atmosphere to obtain the final product. Except the inevitable decomposition of the precursor, there is no other mass loss. Therefore, high-yield product can be harvested.

For investigating the high-power applications of the above products, the rate performance evaluated at different rates is shown in Fig.6(E). Clearly, $CoMoO_4$ MPNSs presented a good rate capability. Specifically, when the current densities were gradually increased to 0.2, 0.4, 1.0, 1.5, 2.0, and 3.0 A/g, the averaged specific capacities of 1384.5, 1280.4, 1148.7, 1110.9, 1002.9 and 810.3 $mA\cdot h\cdot g^{-1}$ could be obtained, respectively. Even up to 4.0 A/g, $CoMoO_4$ MPNSs still delivered an averaged capacity of 540 $mA\cdot h\cdot g^{-1}$. This value is much higher than 372 $mA\cdot h\cdot g^{-1}$(graphite's theoretical capacity). After 70 cycles of high rate testing, once the current density rolled back to 0.2 A/g, the discharge capacity of $CoMoO_4$ MPNSs could still remain at 1372.1 $mA\cdot h\cdot g^{-1}$. For Co-Mo-400, when the testing rates were at 0.2, 0.4, 1.0, 1.5, 2.0, 3.0 and 4.0 A/g, the capacities were around 1417.1, 1211.1, 973.5, 771.4, 621.8, 494.4 and 332.5 $mA\cdot h\cdot g^{-1}$, respectively. These capacities are far below compared with the corresponding ones of $CoMoO_4$ MPNSs. In contrast, Co-Mo-600 and bulk $CoMoO_4$ only exhibited reversible capacities of approximate 173.5 and 58.1 $mA\cdot h\cdot g^{-1}$ upon testing at 4.0 A/g. To study the transport kinetics of electrodes, electrochemical impedance spectroscopy(EIS) detection was carried out. The Nyquist plots of the as-prepared products are revealed in Fig.6(F). The testing frequency range was from 100 kHz to 0.01 Hz. All the measured electrodes were cycled 100 times at 0.2 A/g. As can be seen, each curve has a depressed semicircle and a slope line. The former part belongs to the impedance of charge-transfer, while the latter part belongs to the impedance of solid-state diffusion[38]. Obviously, the charge transfer resistance for $CoMoO_4$ MPNSs is much smaller than those for Co-Mo-400, Co-Mo-600 and bulk $CoMoO_4$. So we can say that $CoMoO_4$ MPNSs possess faster charge-transfer reaction for Li^+ insertion and extraction[20,21].

The stability of the porous sheet structure of $CoMoO_4$ MPNSs is confirmed by SEM(Fig.S7, see the Electronic Supplementary Material of this paper) images of the electrode before and after 100 cycles at a current density of 0.2 A/g. For the fresh electrode[Fig.S7(A)—(C)], the sheet-like structure was broken into smaller pieces due to the sufficiently grinding during the electrode preparation process. However, each piece kept its original morphology, with the nanoparticles in the sheet structure seen clearly. After 100 cycles, as shown in Fig.S7(D)—(I), the sheet structures were still well maintained, indicating the attractive morphological stability.

Ex-situ TEM detections were then carried out to study the nature of the cycling products. The detective cells were first cycled 10 times, and then discharged to 0.01 V or charged to 3.0 V. The corresponding TEM images are presented in Fig.7. Fig.7(A) and (B) show the TEM images of $CoMoO_4$ electrode discharged to 0.01 V, from which it could be seen that the MPNSs was morphology preserved well. Fig.7(C) and (D) are HRTEM images monitored on two separate locations of $CoMoO_4$ MPNSs from Fig.7(B). There show two sets of interlayer distances of 0.222 and 0.205 nm, which fit well with the Mo(110) plane(JCPDS No.42-1120) and Co (111) plane (JCPDS No.15-0806).

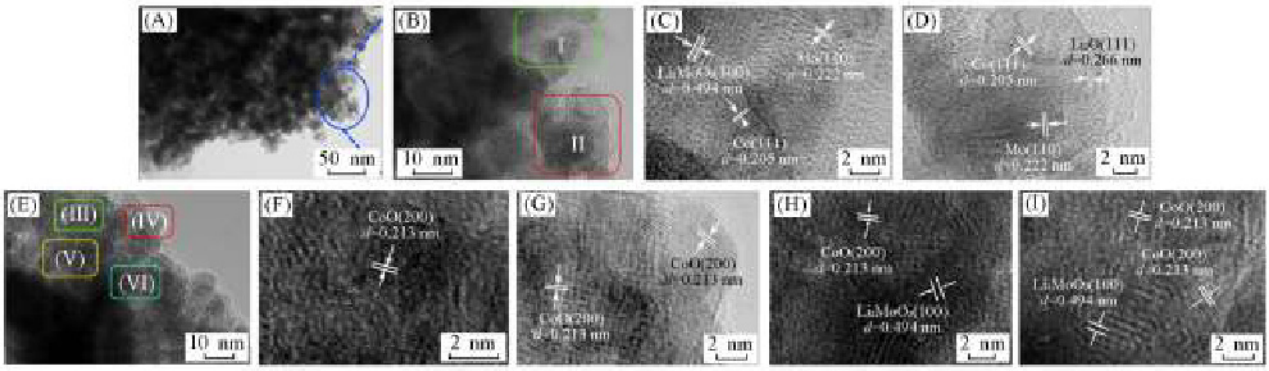

Fig.7 TEM and HRTEM images of $CoMoO_4$ MPNS electrodes collected at the cut-off voltages of 0.01 V(A—D) and 3.0 V(E—I)

(B) The partially magnified SEM image of (A); (C) and (D) HRTEM images for amplifying parts of (I) and (II) in (B); (F)—(I) HRTEM images for amplifying parts of III—VI in (E).

The analyses directly confirm the transformation of $CoMoO_4$ into crystalline Mo and Co, and the results are consistent with Eqs.(1) and (2) mentioned above[38]. Fig.7(D) displays an interplanar distance of 0.266 nm, which belongs to the Li_2O (111) plane(JCPDS No.12-0254). Besides, an interplanar spacing of 0.494 nm could also be observed in Fig.7(C) during this lithiation procedure. This value could be attributed to (100) plane of Li_2MoO_3 phase[JCPDS No.21-0515, Fig.7(C)][38]. We can deduce that the emergence of Li_2MoO_3 is probably due to the multistep lithiation processes of Li^+ insertion into Mo^{6+}. And, furthermore, the as-formed Li_2MoO_3 has not been completely transformed into Mo during the first several cycles.

Upon recharged to 3.0 V, the porous structure of $CoMoO_4$ MPNSs electrode was kept well[Fig.7(E)]. Fig.7(F) and (G) show the HRTEM images for amplifying parts III and IV from Fig.7(E). The 0.213 nm interlayer distance belonged to the CoO (100) plane(JCPDS No.43-1004)[38]. Fig.7(H) and (I) show the

HRTEM images performed on other different areas(Parts V and VI). Surprisingly, besides the 0.213 nm interplanar distance, an interplanar distance of 0.494 nm has also been detected.

To be specific, the former 0.213 nm matches well with the CoO phase, while the latter 0.494 nm could be assigned to the Li_2MoO_3 phase. However, the interlayer distance for MoO_3 has not been detected. This is consistent with the previous report by Chowdari[8]. Although previous reports have shown that the high capacity for $CoMoO_4$ should be closely related with the reformation of MoO_3 during the delithation process. It has been thought that this procedure will promote the uptake as high as 6 mol of Li per unit of the formula. But no evidence has been used to confirm the specific product. Thus there need more refined skills to verify the reformation of MoO_3 from metal Mo.

To further investigate the Li storage mechanism of $CoMoO_4$ MPNSs electrode, *ex situ* XRD measurement was performed at the cutoff voltages of 0.01 and 3 V for the 10th cycle(Fig.8). It should be noted that the very sharp peak at 43.2° in the XRD patterns corresponds to Cu foil. Curve *a* in Fig.8 shows the XRD pattern for the freshly prepared $CoMoO_4$ MPNSs electrode. All the diffraction peaks can be identified as the monoclinic α-$CoMoO_4$(JCPDS No.21-0868). When the $CoMoO_4$ MPNSs electrode was discharged to 0.01 V(curve *b* in Fig.8), the diffraction peaks of $CoMoO_4$ disappeared, indicating initial crystal structure destruction. Meanwhile, the diffraction peaks of LiOH(JCPDS No.32-0564) were detected. In accordance with the forward reaction of Eq.(1), the presence of LiOH can possibly be attributed to the chemical reaction between Li_2O and H_2O in the moist air[33,39]. In contrast, when the $CoMoO_4$ MPNSs electrode was charged to 3.0 V, the peaks of Li_2MoO_4(JCPDS No.12-0763), Li_2MoO_3(JCPDS No.21-0515), $Li_{0.9}Mo_6O_{17}$(JCPDS No.36-0271) and Li_2CO_3(JCPDS No. 21-1141) were found(curve *c* in Fig.8). This suggests the reoxidation of metallic Mo, which agrees well with the TEM results and relevant reports[8]. The XRD patterns of some products are not observable in curves *b* and *c*, such as those of Co^0, Mo^0 and CoO, which might be attributed to the generation of the low crystallinity or small size phases, and this phenomenon has been commonly reported in previous related reports of metal oxide[8,40—43].

Next, a full cell, assembled by $CoMoO_4$ MPNSs anode and $LiFePO_4$ cathode, was performed in order to measure the potential for the application of $CoMoO_4$ MPNSs. The structure schematic of the full cell has been illustrated in Fig.6(G). The full cell voltage curves operated at between 1.6—3.8 V are displayed in Fig.6(H). The first cycle profile shows perfect charge and discharge plateaus at around 3.2 and 2.2 V, displaying a considerable charging/discharging polarization (ΔV was about 1 V). This might be closely related to the sluggish rate of Li^+ diffusion on the $LiFePO_4$ side during the first cycle[33]. The capacities of the discharge and charge processes in the first cycle were 189.6 and 193.1 $mA\cdot h\cdot g^{-1}$ separately, so the initial CE of the full cell was up to 98.2%. The slight capacity loss should be due to the irreversible SEI layer formation and the irreversible decomposition of electrolyte at the $LiFePO_4$ cathode side[38]. From the second cycle on, a sloping potential plateau could be observed clearly from 2.0 V to 3.5 V in the voltage profile and the gap between the charging/discharging plateaus was reduced to 0.2 V. In addition, along with the galvanostatic cycling, the discharge voltage plateaus declined gradually. The structure rearrangement and the polarization action of $CoMoO_4$ MPNSs during the electrochemical cycling were regarded as the primary reasons for the evident voltage platform drop[44]. The full cell was cycled at 0.1C, and the cycling curves and corresponding CE are displayed in Fig.6(I). As can be seen, a stable discharge capacity of 146.7 $mA\cdot h\cdot g^{-1}$ was obtained after 50 cycles, corresponding to a 77.4% capacity retention. Besides, the CE values were stabilized over 98% after the second cycle, demonstrating the high efficiency of the full cell. Moreover, the capacity comparisons of the $LiFePO_4$/$CoMoO_4$ full cell with reported ones of $CoMoO_4$-based, Co-based, Mo-based, and those heterojunction materials are also listed in the Table S1(see the Electronic Supplementary Material of this paper). Clearly, the full cell in our work showed a better property in terms of cyclability and specific capacity, proving the potential of $CoMoO_4$ MPNSs as an anode material for Li-batteries.

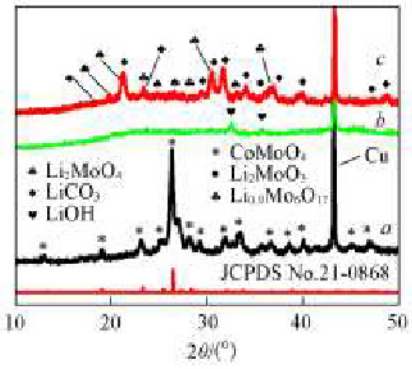

Fig.8 XRD patterns of fresh $CoMoO_4$ MPNSs electrode(*a*), discharged to 0.01 V(*b*), and charged to 3.0 V(*c*)

On the basis of the above results, the good Li-storage properties of $CoMoO_4$ MPNSs are attributed to their unique structural features, as illustrated in Scheme 1. Specifically, $CoMoO_4$ MPNSs with small size nanocrystals[Fig.1(A)—(D)] can offer short transmission routes for lithium ion/electron and accelerate reversible insertion/extraction of lithium, thus leading to a good rate capability[Fig.6(E)]. In addition, the mesoporous structure of $CoMoO_4$ MPNSs will enlarge the electrolyte-electrode contact area and benefit the penetration of electrolyte, resulting in more active sites(Fig.3). Moreover, the porous structure can accommodate large mechanical strains by providing the cavity to alleviate the volume change during the repeated inserting/extracting process. Also the robust sub-micrometer sheet-like structure will prevent the NPs from aggregation, guarantee the electrode integrity[Fig.7(A) and Fig.S7], and enhance the capacity retention upon prolonged cycling[Fig.6(D)]. In a word, these findings indicate that the microstructure design of materials plays a key role in strengthening their electrochemical properties both in half and full Li-storage cells.

4 Conclusions

A simple and scalable freeze drying assisted strategy for fabricating $CoMoO_4$ MPNSs has been performed. In contrast to bulk $CoMoO_4$ and other reported $CoMoO_4$ materials, the resultant $CoMoO_4$ MPNSs exhibit exceptional Li-storage properties in terms of cycle stability, specific capacity and rate capability. The robust sheet-like structure owns abundant hierarchical pores, which can alleviate the volumetric expansion stress and offer fast Li^+ and e^- transport path, thus yielding a nice Li-storage performance. Furthermore, a specific capacity of 189.6 $mA{\cdot}h{\cdot}g^{-1}$ was achieved by the $LiFePO_4/CoMoO_4$ MPNSs full cell and a capacity retention of 77.4% was obtained over 50 cycles. With the novel microstructure design and the ease fabrication considered, such a strategy would broaden the viewing angle in the synthetic methodology of mesoporous structures for lithium ion batteries.

Electronic Supplementary Material

Supplementary material is available in the online version of this article at http://dx.doi.org/10.1007/s40242-019-8316-1.

References

[1] Xin T., Diao F. Y., Li C., Feng H. L., Liu G. J., Zou J. J., Ding Y. H., Liu B., Wang Y. Q., *Mater. Res. Bull.,* **2018**, *99*, 196

[2] Zou J. J., Liu B., Liu H. Q., Ding Y. H., Xin T., Wang Y. Q., *Mater. Res. Bull.,* **2018**, *107*, 468

[3] Ding Y. H., Liu B., Zou J. J., Liu H. Q., Xin T., Xia L. H., Wang Y. Q., *Mater. Res. Bull.,* **2018**, *106*, 7

[4] Wang C., Wu L. X., Wang H., Zuo W. H., Li Y. Y., Liu J. P., *Adv. Funct. Mater.,* **2015**, *25*, 3524

[5] Wang Z. Y., Madhavi S., Lou X. W., *J. Phys. Chem. C,* **2012**, *116*, 12508

[6] Sakaushi K., Thomas J., Kaskel S., Eckert J., *Chem. Mater.*, **2013**, *25*, 2557

[7] Ahn J. H., Park G. D., Kang Y. C., Lee J. H., *Electrochim. Acta*, **2015**, *174*, 102

[8] Cherian C. T., Reddy M. V., Haur S. C., Chowdari B. V. R., *ACS Appl. Mater. Interfaces*, **2013**, *5*, 918

[9] Xue R. N., Hong W., Pan Z., Jin W., Zhao H. L., Song Y. H., Zhou J. K., Liu Y., *Electrochim. Acta*, **2016**, *222*, 838

[10] Wei H. X., Yang J., Zhang Y. F., Qian Y., Geng H. B., *J. Colloid Interf. Sci.*, **2018**, *524*, 256

[11] Zhang L. F., He W. J., Ling M., Shen K. C., Liu Y., Guo S. W., *Electrochim. Acta,* **2017**, *252*, 322

[12] You J. F., Xin L., Yu X., Zhou X., Liu Y., *Appl. Phys. A*, **2018**, *124*, 271

[13] Ju Z. C., Zhang E., Zhao Y. L., Xing Z., Zhuang Q. C., Qiang Y. H., Qian Y. T., *Small*, **2015**, *11*, 4753

[14] Liu H. W., Tan L., *Ionics,* **2010**, *16*, 57

[15] Ding Y., Wan Y., Min Y. L., Zhang W., Yu S. H., *Inorg. Chem.*, **2008**, *47*, 7813

[16] Yu H., Guan C., Rui X. H., Ouyang B., Yadian B. L., Huang Y. Z., Zhang H., Hoster H. E., Fan H. J., Yan Q. Y., *Nanoscale*, **2014**, *6*, 10556

[17] Ko Y. N., Kang Y. C., Park S. B., *RSC Adv.*, **2014**, *4*, 17873

[18] Kim J. K., Kim J. H., Kang Y. C., *Chem. Eng. J.*, **2018**, *333*, 665

[19] Wang Y. S., Sun Y. F., Zhang X., Wen Y. H., Guo J. X., *RSC Adv.*, **2016**, *6*, 51710

[20] Yao J. Y., Gong Y. J., Yang S. B., Xiao P., Zhang Y. H., Keyshar K., Ye G. L., Ozden S., Vajtai R., Ajayan P. M., *ACS Appl. Mater. Interfaces*, **2014**, *6*, 20414

[21] Yang T., Zhang H. N., Luo Y. Z., Mei L., Guo D., Li Q. H., Wang T. H., *Electrochim. Acta*, **2015**, *158*, 327

[22] Guo J. X., Zhu H. F., Zhou S. Q., Sun Y. F., Zhang X., *Ionics*, **2015**, *21*, 2993

[23] Xu J., Gu S. Z., Fan L., Xu P., Lu B., *Electrochim. Acta*, **2016**, *196*, 125

[24] Lyu D. H., Zhang L. L., Wei H. X., Geng H. B., Gu H. W., *RSC Adv.*, **2017**, *7*, 51506

[25] Chen Y. P., Liu B. R., Jiang W., Liu Q., Liu J. Y., Wang J., Zhang H. S., Jing X. Y., *J. Power Sources*, **2015**, *300*, 132

[26] Wang B., Li S. M., Wu X. Y., Liu J. H., Tian W. M., Chen J., *New J. Chem.*, **2016**, *40*, 2259

[27] Yang Y., Wang S. T., Jiang C. H., Lu Q. C., Tang Z. L., Wang X., *Chem. Mater.,* **2016**, *28,* 2417

[28] Wang Y. X., Wu Y., Xing L. L., Wang Q., Xue X. Y., *J. Alloy. Compd.*, **2016**, *689*, 655

[29] Chen Y. Y., Wang Y., Shen X. P., Cai R., Yang H. X., Xu K. Q., Yuan A. H., Ji Z. Y., *J. Mater. Chem. A*, **2018**, *6*, 1048

[30] Zhang L., Zheng S. S., Wang L., Tang H., Xue H. G., Wang G. X., Pang H., *Small*, **2017**, *13*, 1700917

[31] Wang H., Liu X. Y., Chuah Y. J., Goh J. C. H., Li J. L., Xu H. Y., *Chem. Commun.*, **2013**, *49*, 1431

[32] Wang W., Sun Y., Liu B., Wang S. G., Cao M. H., *Carbon*, **2015**, *91*, 56

[33] Wang W., Qin J. W., Cao M. H., *ACS Appl. Mater. Interfaces*, **2016**, *8*, 1388

[34] Cui Z. T., Wang S. G., Zhang Y. H., Cao M. H., *Electrochim. Acta*, **2015**, *182*, 507

[35] Yin Z. Y., Zhang X., Cai Y. Q., Chen J. Z., Wong J. I., Tay Y. Y., Chai J. W., Wu J., Zeng Z. Y., Zheng B., Yang H. Y., Zhang H., *Angew. Chem. Int. Ed.*, **2014**, *53*, 12560

[36] Lei F. C., Sun Y. F., Liu K. T., Gao S., Liang L., Pan B. C., Xie Y., *J. Am. Chem. Soc.,* **2014**, *136*, 6826

[37] Adamski P., Moszyński D., Komorowska A., Nadziejko M., Sarnecki A., Albrecht A., *Inorg. Chem.*, **2018**, *57*, 9844

[38] Wang W., Qin J. W., Yin Z. G., Cao M. H., *ACS Nano,* **2016**, *10*, 10106

[39] Hy S., Felix F., Rick J., Su W. N., Wang B. J. H., *J. Am. Chem. Soc.,* **2014**, *136*, 999

[40] He Y. Y., Li A. H., Dong C. F., Li C. C., Xu L. Q., *Chem. Eur. J.*, **2017**, *23*, 13724

[41] Jin S. X., Yang G. Z., Song H. W., Cui H., Wang C. X., *ACS Appl. Mater. Interfaces*, **2015**, *7*, 24932

[42] Ang W. A., Cheah Y. L., Wong C. L., Prasanth R., Hng H. H., Madhavi S., *J. Phys. Chem. C*, **2013**, *117*, 16316

[43] Sharma Y., Sharma N., Subba Rao G. V., Chowdari B. V. R., *Adv. Funct. Mater.,* **2007**, *17*, 2855

[44] Popovic J., Demir Cakan R., Tornow J., Morcrette M., Su D. S., Schlögl R., Antonietti M., Titirici M. M., *Small*, **2011**, *7*, 1127